A SIMULTANEOUS APPLICATION OF PLIF-PIV-PTV FOR THE DETAILED EXPERIMENTAL STUDY OF THE HYDRODYNAMIC CHARACTERISTICS OF THIN FILM FLOWS

Charogiannis A.[1], Denner F.[2], Pradas M.[1], Kalliadasis S.[1] van Wachem B.G.M.[2] and Markides C.N.[1]*
*Author for correspondence
Department of Chemical Engineering[1], Department of Mechanical Engineering[2]
Imperial College London, London, SW7 2AZ, United Kingdom,
E-mail: c.markides@imperial.ac.uk

ABSTRACT

Films falling over flat inclined plates are employed over a broad range of industrial applications owing to their superior heat and mass transfer capabilities. However, and despite extensive research efforts, many aspects of the dynamics of the particular class of interfacial flows still elude us. This paper reports on the application of Laser-Induced Fluorescence imaging alongside simultaneous Particle Image/Tracking Velocimetry to isothermal, harmonically excited, gravity-driven liquid films, in order to spatiotemporally resolve the flow field underneath the wavy interface. Results generated using this experimental methodology are expanded to provide information on spatiotemporally resolved mass transfer characteristics and pursue comparisons to analytically derived estimates. The latter are observed to severely overestimate the experiments depending on flow conditions and wave topology. Finally, the effect of unsteadiness is brought into focus by decomposing the time-varying flow rate into mean and fluctuating components. The latter is shown to vary linearly with the variance of the film thickness for each of the two liquids presently examined.

INTRODUCTION

The present paper is dedicated to an experimental investigation of isothermal, harmonically excited, gravity-driven liquid films flowing over a flat inclined plate. Owing to their high surface-to-volume ratios and superior heat and mass transfer capabilities, such films are employed in a broad range of industrial applications, including wetted-wall absorbers, condensers, evaporators and reactors. It comes as no surprise, therefore, that extensive theoretical [1], experimental [2] and numerical [3] efforts have been devoted to relevant studies since the first systematic work was published by Kapitza and Kapitza [4].

Despite the extensive body of previous experimental work, only a limited number of publications relating to simultaneous spatiotemporal variations of the film thickness and velocity in the flows of interest is available; an observation inherently linked to the restricted liquid domain under observation and the intermittent nature of the moving and wavy interface that makes such measurements particularly challenging. Nevertheless, recent efforts utilizing advanced optical techniques such as Chromatic Confocal Imaging (CCI), Laser-Induced Fluorescence (LIF), Particle Image/Tracking Velocimetry (PIV/PTV) and micro-PIV have enhanced our understanding of the underlying complex flow phenomena. For example, Dietze and co-workers [5, 6] (using CCI and micro-PIV) were the first to experimentally observe backflow in the capillary wave regions, Adomeit and Renz [7] (using micro-PIV) noted deviations from Nusselt velocity profile predictions depending on film topology, and Zadrazil and Markides [8, 9] (using LIF and PIV) observed multiple recirculation zones within disturbance waves in downwards annular flows.

Despite such novel insights, a comprehensive study linking spatiotemporally resolved flow field measurements to the mass transfer characteristics of films flows is still lacking; the present paper, therefore, aims to fulfil this requirement. In greater detail, the paper reports on an application of LIF imaging alongside simultaneous PIV and PTV to falling, planar thin-film flows in order to spatiotemporally resolve the flow field underneath the wavy interface. The results from this approach, whose original development was reported in Ref. [11] and which is extended here to provide information on spatiotemporally resolved mass transfer characteristics, can offer powerful insights into the hydrodynamics of the particular class of interfacial flows, while generating useful validation data for advanced modelling efforts.

NOMENCLATURE

D	[m]	Characteristic dimension for the *Re* number definition
f	[s^{-1}]	Forcing/wave frequency
g	[m/s^2]	Gravitational acceleration
Ka	[-]	Kapitza number
Q	[m^3/s]	Steady flow rate
Q'	[m^3/s]	Unsteady flow rate
Re	[-]	Reynolds number
t	[s]	Time
ν	[m^2/s]	Kinematic viscosity
w	[m]	Film span
x	[m]	Distance along the film
y	[m]	Distance from the wall

Special characters

β	[°]	Film inclination angle
Γ	[m^2/s]	Flow rate per unit width of the flow
δ	[m]	Film thickness
ρ	[kg/m^3]	Density
σ	[N/m]	Surface tension

Subscripts

b	Bulk: Referring to velocity
box	Flow distribution box
f	Fluid
N	Nusselt: Referring to the Nusselt solution
std	Standard deviation

Overall, the experimental campaign comprises four different Kapitza (*Ka*) number liquids (aqueous glycerol solutions), Reynolds (*Re*) numbers spanning the 2 - 320 range, and inlet forcing frequencies between 1 and 10 Hz. In this contribution, presented results will be limited to select conditions, mainly focusing on the effect of unsteadiness on the mass transport characteristics of the examined films, as well as on comparisons with analytical calculations. The definitions of two primary experimental parameters, namely the *Re* and *Ka* numbers are given in Equations (1) and (2). *Ka* represents the dimensionless ratio of surface tension to inertial forces, and stands for an indicator of the hydrodynamic wave regime.

$$Re = \frac{DU}{\nu_f} \tag{1}$$

$$Ka = \frac{\sigma_f}{\rho_f \nu_f^{4/3} (g \sin\beta)^{1/2}} \tag{2}$$

EXPERIMENTAL SETUP

A detailed description of the experimental setup can be found elsewhere [10], yet a synopsis is provided here for completion. The liquid circulates within a closed loop comprising a 0.7 mm thick, 400×285 mm soda lime glass plate over which the desired film flows develop (Figure 1).

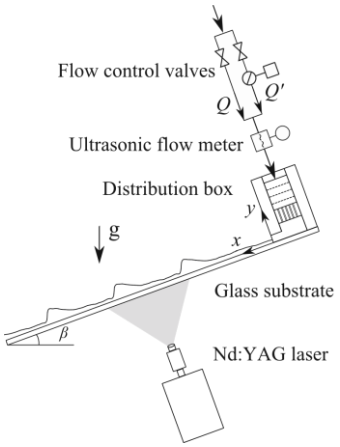

Figure 1 Schematic of the experimental test section.

The plate itself is mounted on an aluminium frame inclined at $\beta = 20°$ to the horizontal, while a distribution box has been installed in order to uniformly dispense the flow over the plate and minimise turbulence at the inlet. The box outlet has been equipped with a knife-edge, the height of which is adjusted to regulate the flow contraction and prevent the generation of a hydraulic jump or any backflow. Using the mean flow rate measurement from an ultrasonic flowmeter installed at the box supply, a *Re* number can be defined as in Equation (3), where U_{box} stands for the velocity, *D* for the channel depth (20 mm) and Γ for the flow rate per unit width of the channel (285 mm).

$$Re = \frac{DU_{box}}{\nu_f} = \frac{\Gamma}{\nu_f} \tag{3}$$

Upstream of the distribution box, the flow is split into a steady (*Q*) and a pulsating supply (*Q´*), the latter generated using a rotating valve, allowing for accurate control of both wave frequency and amplitude. In this way, fully developed wave regimes were obtained within the confines of a short test section. Excitation of the dye and particle seeded flow was performed from the wall side (i.e., from underneath) using a double-cavity frequency-doubled Nd:YAG laser (100 Hz). This avoided illuminating the liquid from the wavy interface, which would have subjected the laser sheet (approximately 200 μm thick) to strong, spatially and temporally non-uniform distortions and lensing. Imaging was also carried out from below so as to limit image distortions. The imaging setup comprises a pair of LaVision VC-Imager Pro HS 500 CMOS cameras equipped with Sigma 105 mm f/2.8 Macro lenses and extension rings (32 mm) in order to achieve the desired magnification. Both cameras and lasers were synchronized by a LaVision High Speed Controller (HSC) and operated using the LaVision Davis 8.2.1 software.

Variations to the *Ka* number, which constitutes one of our primary objectives, can be imposed by tailoring the liquid viscosity and density; therefore the implementation of a novel refractive index correction tactic was necessary [11]. In particular, the imaging planes of both cameras were mapped and corrected for perspective distortions using a calibration graticule immersed inside the employed liquid solution, and a pinhole model available in Davis. To this end, a Perspex box with its bottom surface removed (the one that would otherwise adhere to the glass) was carefully positioned at the excitation plane using a micrometer stage and subsequently filled with the liquid. The apparent resolution for the presently examined *Ka* numbers was between 28.0 and 29.7 μm/pixel, with the fit root mean square (RMS) errors ranging between 0.5 and 0.9 pixels and the imaging domain along the film extending to approximately 33 mm. A short-pass filter with a cut-off frequency at 550 nm was installed on the PIV camera, while a long-pass filter with a 540 nm cut-off frequency was used for LIF. The dye (Rhodamine B) concentration was approximately 0.5 g/L, while glass hollow spheres (11.7 μm mean diameter) were seeded at a concentration of approximately 0.18 g/L for tracking the fluid motion.

EXPERIMENTAL METHOD

Both cameras were operated in dual-frame mode, so that for every PIV frame a corresponding LIF frame was acquired. The interframe separation was varied between 0.45 and 1.50 ms, allowing for particle displacements of 8 – 15 pixels at the interface. A sample perspective distortion corrected LIF frame along with its processed counterpart are presented in Figure 2. Close inspection of raw LIF images reveals that the fluorescence emitted by the film is reflected about the gas-liquid interface, while reflections by the glass substrate blur the LIF signal locally. The location of the solid-liquid interface was obtained directly from the LIF images using an edge detection algorithm [12], while with respect to the gas-liquid interface, intercepts between linear fits to maximum signal gradients and reflection intensity profiles were employed as estimates of the liquid boundary. Compared to alternative tactics that were considered, based on a threshold intensity and a maximum gradient intercept with the zero intensity axis approaches, the selected method produced smoother results and was more robust in regions with locally stronger reflections.

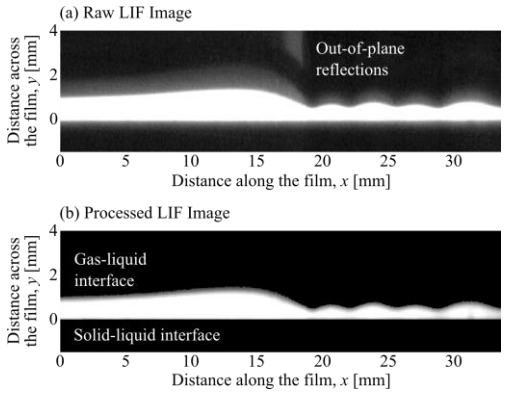

Figure 2 (a) Refractive index and perspective distortion corrected LIF image, and (b) corresponding fully processed LIF image, for a film flow with Re = 129.4, Ka = 1799, f_w = 10 Hz.

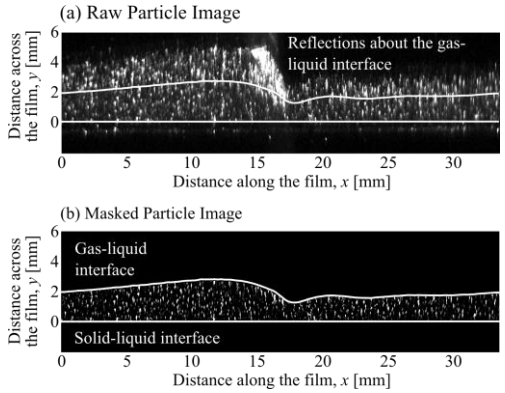

Figure 3 (a) Refractive index and perspective distortion corrected particle image, and (b) corresponding fully processed image, for a film flow with Re = 26.93, Ka = 84.87, f_w =10 Hz.

Similarly to the LIF images, reflections of primary scattered signals from to the entire illuminated liquid volume appeared above the gas-liquid interface in the raw PIV images (Figure 3 (a)). In this case, however, the reflection intensities were comparable to the original signals, rendering the identification of secondary scattering sources as such, highly non-trivial. Thus, binarized LIF images were imported in Davis and used to mask out any regions associated with out-of plane reflections. The masked particle images were then used to generate two-dimensional velocity vector maps by means of a four-pass cross-correlation approach. For the first and second passes, a 32×32 pixel interrogation window was selected with a 50% overlap. For the third and fourth passes, the interrogation window was reduced to 16×16 pixels. The resulting vector-to-vector PIV spatial resolution is estimated as being between 222.4 and 236.6 μm, depending on the experimental round. Finally, individual particles were tracked (PTV calculation) by employment of the obtained PIV results as reference estimators of the velocity field. A comprehensive account of all processing steps employed in the LIF, PIV and PTV vector field calculations can be found in Ref. [13]. PTV, rather than PIV was favoured in the present study due to the superior spatial resolution on offer, as well as the reduced propensity towards bias errors in the presence of gradients [14].

In order to examine the velocity distributions underneath the waves in detail, the practice of phase-averaging PTV maps corresponding to the same spatial domain was adopted. The primary challenge was to identify which images could be averaged out and by how much each would need to translated in the axial direction so as to match the desired topology. A film thickness profile (reference signal) pertaining to the desired topology was initially selected and cross-correlated with all available thickness traces from the same data set. Signal pairs satisfying a maximum displacement condition (80 pixels) where repositioned and averaged, as where the corresponding PTV images (Figure 4).

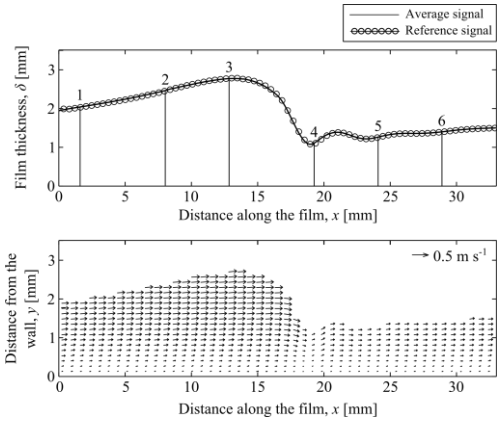

Figure 4 (Top) Phase-averaged wave profile (and reference wave-locations; see Figure 5) for a liquid-film flow with Re = 26.93, Ka = 84.87 and f_w = 10 Hz. (Bottom) Corresponding average liquid-phase PTV velocity field for the same flow.

A series of experiments were conducted in order to assess the validity of the combined optical methodology. First, film thicknesses from flat (unforced) films (Ka = 14.06) were compared to micrometer stage measurements, as well as the one-dimensional, steady, fully developed solution of the Navier-Stokes equation under the assumption of negligible inertia, also known as the Nusselt solution [15]. The resulting deviations were around 20 μm for both tests; less than the apparent image resolution. Relative deviations were calculated between PTV derived interfacial and bulk velocities and analytical results, with mean values amounting to 3.2% for both test cases, while flow rate comparisons were conducted between LIF/PTV derived and flowmeter data. The mean relative deviation was 1.6% for a total of six flat and nine wavy flows. The Nusselt expressions for the film thickness δ_N, and bulk velocity U_{Nb}, are given below (these will be employed later on in comparisons with optical measurement results).

$$\delta_N = \left(\frac{3\nu_f Q}{g w \sin\beta} \right)^{1/3} \tag{4}$$

$$U_{Nb} = \frac{g \sin\beta \delta_N^{\,2}}{3\nu_f} \tag{5}$$

TRENDS AND RESULTS

Velocity Profiles

By implementing the previously described experimental methodologies and processing steps, the flow field underneath

the wavy liquid-air interface can be examined for a broad range of harmonically excited films, including direct comparisons to analytical calculations. A similar analysis attempted by other researchers [7, 16], though to our knowledge only for unforced film flows, concentrated on axial velocity profile comparisons to analytically derived ones. Effectively, results from the Nusselt solution are compared to experimentally derived ones for the flow field behind, underneath, and ahead of the wave crest. It is noted that these calculations are based on the experimentally derived film thickness data. By inspection of the results in Figure 5 (corresponding to the numbered locations along the wave in Figure 4), it is evident that the analytical prediction nearly matches the experiment behind the wave crest, significantly overestimates it in close vicinity to the wave crest, and slightly underestimates it in the capillary wave zone, in agreement with earlier observations in Refs. [7, 16]. In more detail, the absolute deviations between the experimentally derived and calculated interfacial velocities amount to less than 10% at Location 1, around 35% at Location 2, 70% at Location 3, nearly 15% at Location 4, and approximately 25% at Locations 5 and 6. Both the trend and deviation magnitudes agree well with results published in Ref. [16] for a *Re* = 16 and *Ka* = 18.54 laminar film falling down a 45° inclined plate.

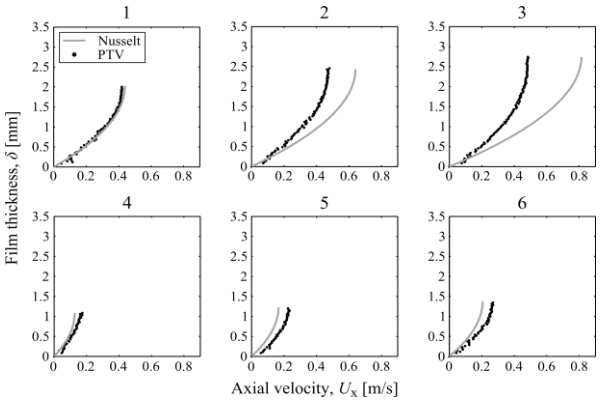

Figure 5 Experimental (PTV) and analytically derived (Nusselt solution) axial velocity profiles corresponding to the six numbered wave-locations indicated in Figure 4 (top).

Flow Rates

The preceding analysis was then expanded to allow for flow rate comparisons between waves from different flows, as well as their analytically derived counterparts. In more detail, each axial velocity profile along an averaged PTV map, such as the one previewed in Figure 4, was integrated using the trapezoidal rule and multiplied by the local film thickness and film span. For the same film height values, bulk velocities were calculated using the corresponding Nusselt relationship yielding flow rate predictions. Sample results are shown in Figure 6.

Despite the fact that different *Ka* and *Re* flows were selected for the particular comparative assessment, the mean flow rates for all three flows are nearly identical (within 5%). For the *Ka* = 14.06 flow, deviations between experiments and analytically calculated results are small, with the mass carrying capacity of the wave being slightly lower than the analytical results suggest, and the flow rate ahead of the wave being slightly underestimated. As the *Ka* number increases the aforementioned trend persists; however, the deviation near the wave crest increases to nearly 65%. For the *Ka* = 346.2 flow, the calculated flow rate at wave the crest exceeds the experimental value by more than 100%.

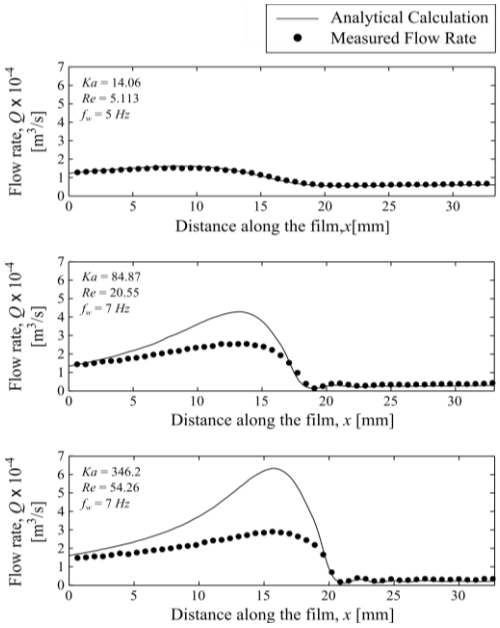

Figure 6 Flow rate comparisons between experiments and analytical calculations for waves in flows with *Ka* = 14.06 (top), *Ka* = 84.87 (middle), and *Ka* = 346.2 (bottom) liquids.

An equivalent analysis was pursued for time-varying flow rate results generated using the following approach: film thickness data were averaged along a 1.8 mm region of the flow on a per image basis, while averaged axial velocity profiles were generated over the same spatial domain and subsequently integrated over the liquid domain. Thus, every LIF/PTV image pair contributed a single, local and instantaneous flow rate measurement; upon averaging all individual flow rates over an entire data set corresponding to a fixed flow condition, a mean flow rate can be obtained and compared to the flow meter measurement for validation purposes. The latter were found to deviate by only 2.1% on average over 50 studied flow comparisons.

Flow rate time traces (over one second) are presented in Figure 7 for flows with *Ka* = 84.87 and *Re* = 10.64, 14.29, 20.55 and 24.72, alongside complementary analytical results. The latter once again stem from bulk velocity estimates generated using experimentally derived local film thickness data. As the *Re* number increases, this time by increasing the flow rate, the deviations between experiments and analytical results grow in a similar fashion to the one observed earlier; films characterized by stronger flow rate fluctuations display higher deviations. Also in agreement with the previous assessment, absolute deviations peak in close vicinity to the wave crests. It is therefore evident from the so-far presented results that the examined analytical approach fails to reproduce the experimentally obtained data, as the velocities underneath the waves fall significantly short of the values expected from theoretical analyses relying on the Nusselt solution.

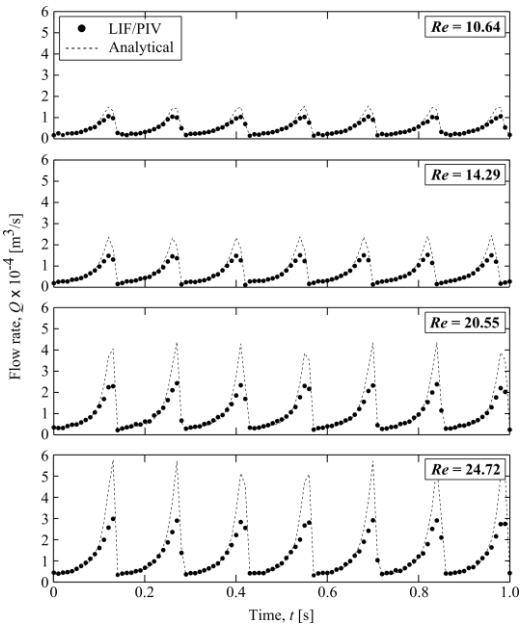

Figure 7 Flow rate time traces over 1 s obtained from simultaneously conducted LIF and PTV measurements, and presented along with complementary analytical results.

Mass transfer characterization

The impact of unsteadiness on the mass carrying capacity of harmonically excited film flows can be examined more rigorously by a Reynolds decomposition of the time-varying flow rate into mean and fluctuating components:

$$Q = \overline{Q} + Q' \tag{6}$$

Equation (6) can be normalized by the span (which is constant) and expanded into a function that includes the mean and fluctuations of the bulk velocity and film thickness:

$$\overline{Q} = \overline{U_\mathrm{b}}\,\overline{\delta} + \overline{U_\mathrm{b}'\delta'} \tag{7}$$

The first term in Equation (7), hereby referred to as the "steady term", is the product of the time-averaged bulk velocity and film thickness, and corresponds to the flow rate of an equivalent *steady* film flow (without waves) that has a bulk velocity and thickness equal to the averaged bulk velocity and thickness of the actual flow under investigation. The second term, designated the "unsteady term", is the covariance (time-averaged product) of the two fluctuating terms, and represents the coupling between the local and instantaneous film thickness and velocity. For a flat film (where the flow rate is constant) the unsteady term is equal to zero and the mean bulk velocity calculation is straightforward. The introduction of waviness (Figure 8) entails a non-zero unsteady term and a consequent deviation between the analytical calculation and experiment; the time-averaged U_b is overestimated due to significant velocity deviations underneath the waves, which grow with increasing unsteadiness (stronger flow rate fluctuations).

In consequence of these observations, an alternative approach to the experimental-analytical comparative studies so far conducted has been pursued and is hereby presented. Going back to the flow rate breakdown of Equation 7, the LIF and PTV results allow us to calculate time-averaged flow rates (Q), as well as time-averaged U_b and δ values; unsteady terms can then be obtained directly from Equation 7. For the same experimentally derived time-varying flow rate trace, film thicknesses and bulk velocities can be calculated at each measurement point using the Nusselt expressions. If processed in the same manner as the experimental results, steady and unsteady terms can be generated. This approach was implemented over a total of 46 flows, 21 originating from the *Ka* = 346.2 data set, and 26 from the *Ka* = 84.87 data set. Based on the results of this analysis, shown in Figures 8 and 9, the following remarks can be made:

1. Analytical predictions consistently match the experimentally retrieved steady terms, with a mean absolute deviation of 0.77%. This is evidenced by the corresponding data point overlap in Figure 8.
2. The steady term scales linearly with *Re* for each of the two *Ka* data sets; a relatively unsurprising outcome given that both mean bulk velocity and thickness are included in the film *Re* definition.
3. For the *Ka* = 84.87 flows, the ratio of unsteady to steady terms increases with increasing *Re* and then falls off at around *Re* = 20, spanning the range 2.2% - 12.44%.
4. Regarding the *Ka* = 346.2 data, increasing the *Re* consistently results in a reduction in the relative magnitudes of the unsteady terms. The latter are, however, considerably higher compared to the *Ka* = 84.87 flows, ranging from 7.8% to 25%.
5. An inverse trend is observed between the ratio of unsteady to steady terms and the wave frequency; from 5 to 7 and then to 10 Hz, relative unsteady terms diminish (*Ka* = 84.8). The same trend is observed for the *Ka* = 346.2 flows (only 7 Hz and 10 Hz cases were examined for the particular liquid solution).
6. The mean deviation between experimentally obtained and analytically derived unsteady terms, over all examined flow conditions, is 7.5%. It may be speculated that this deviation is linked to the one noted earlier regarding the steady terms, although this requires further work to ascertain.
7. Finally, for both *Ka* number liquids, the unsteady term scales linearly with the variance of the film thickness, effectively a measure of film waviness (Figure 9).

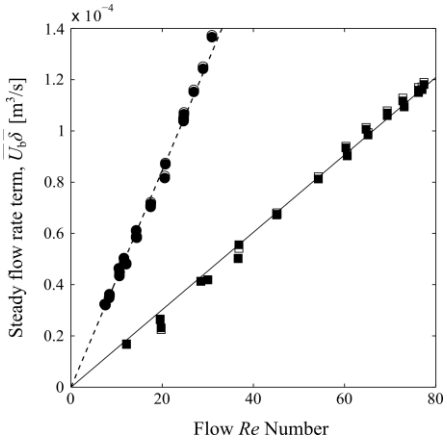

Figure 8 Steady flow rate terms for flows with *Ka* = 84.87 and *Ka* = 346.2 as a function of the flow *Re*. For legend see Figure 9.

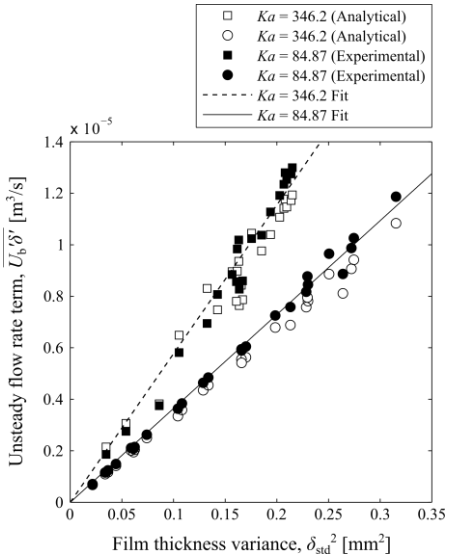

Figure 9 Unsteady flow rate terms for flows with *Ka* = 84.87 and *Ka* = 346.2 against corresponding film thickness variances.

CONCLUSION

The deviations observed in flow rate comparisons between waves from different flows and their analytically derived counterparts are linked to the wave topology. With increasing *Ka* and *Re* numbers, the wave mass carrying capacity is increasingly overestimated by the analytical calculation, with deviations exceeding 100% near the wave crest. In contrast, analytically calculated velocity profiles behind the crest agree well with experiments, while ahead of the wave crest, the latter typically exhibit lower velocities than the experimentally observed ones. Along with the comparative analysis carried out for phase-averaged wave profiles, time-varying flow rate comparisons were pursued, with the results suggesting that films characterized by stronger flow rate fluctuations display consistently higher deviations. Also in agreement with the previous assessment, absolute deviations peak in close vicinity to the wave crests.

As the examined analytical approach failed to reproduce the experimentally obtained data, the impact of unsteadiness on the mass carrying capacity of harmonically excited films was examined by a Reynolds decomposition of the time-varying flow rate into mean and fluctuating components. In that case, analytical predictions consistently matched the steady terms (product of the time-averaged bulk velocity and thickness), which scaled linearly with the *Re* number. Close agreement (mean deviation of 7.5%) was also observed between experimentally and analytically derived unsteady terms (covariance of the fluctuating thickness and bulk velocity), which were found to scale linearly with the film thickness variance, effectively a measure of film waviness.

ACKNOWLEDGEMENTS

This work was supported by the Engineering and Physical Sciences Research Council (EPSRC), UK [grant number EP/K008595/1].

REFERENCES

[1] Pradas, M., Tseluiko, D. and Kalliadasis, S., Rigorous coherent-structure theory for falling liquid films: Viscous dispersion effects on bound-state formation and self-organization, *Phys. Fluids*, Vol. 23, 2011, pp. 044104-1-19

[2] Mathie, R., Nakamura, H. and Markides, C. N., Heat transfer augmentation in unsteady conjugate thermal systems - Part II: Applications, *Int. J. Heat Mass Transfer*, Vol. 56, 2013, pp. 819-833

[3] Rohlfs, W. and Scheid, B., Phase diagram for the onset of circulating waves and flow reversal in inclined falling films, *J. Fluid Mech.*, Vol. 763, pp. 322-352

[4] Kapitza, P. L., Wave flow of thin layers of a viscous fluid: I. Free flow, *Zhurnal Eksperimentalnoi I Teoreticheskoi Fiziki*, Vol. 18, 1948, pp. 3-18

[5] Dietze, G. F., Al-Sibai, F. and Kneer, R., Experimental study of flow separation in laminar falling liquid films, *J. Fluid Mech.*, Vol. 637, 2009, pp. 73-104

[6] Dietze, G. F., Leefken, A. and Kneer, R., Investigation of the backflow phenomenon in falling liquid films, *J. Fluid Mech.*, Vol. 595, 2008, pp. 435-459

[7] Adomeit, P. and Renz, U., Hydrodynamics of three-dimensional waves in laminar falling films, *Int. J. Multiphase Flow*, Vol. 26, 2000, pp. 1183-1208

[8] Zadrazil, I., Matar, O. K. and Markides, C. N., An experimental characterization of downwards gas-liquid annular flow by laser-induced fluorescence: Flow regimes and film statistics, *Int. J. Multiphase Flow*, Vol. 60, 2014, pp. 87-102

[9] Zadrazil, I., Matar, O. K. and Markides, C. N., An experimental characterization of liquid films in downwards co-current gas-liquid annular flow by particle image and tracking velocimetry, *Int. J. Multiphase Flow*, Vol. 68, 2014, pp. 1-12

[10] Charogiannis, A. and Markides, C. N., Experimental Study of Falling Films by Simultaneous Laser-Induced Fluorescence, Particle Image Velocimetry and Particle Tracking Velocimetry, *17th International Symposium on Applications of Laser Techniques to Fluid Mechanics, Lisbon, Portugal*, 2014

[11] Budwig, R., Refractive index matching methods for liquid flow investigations, *Exp. Fluids*, Vol. 17, 1994, pp. 350-355

[12] Zhu, Y. M., Kaftandjian, V., Peix, G. and Babot, D., Modulation transfer function evaluation of linear solid-state x-ray-sensitive detectors using edge techniques, *Appl. Opt.*, Vol. 34, 1995, pp. 4937-4943

[13] Charogiannis, A., An, J. S. and Markides, C. N., A Simultaneous Laser-Induced Fluorescence, Particle Image Velocimetry and Particle Tracking Velocimetry Technique for the Investigation of Liquid Film Flows, *Exp. Therm. Fluid Sci., submitted, in peer review*

[14] Kähler, C. J., Scharnowski, S. and Cierpka, C., On the uncertainty of digital PIV and PTV near walls, *Exp. Fluids*, Vol. 52, 2012, pp. 1641-1656

[15] Nusselt, W., Die Oberflachenkondensation des Wasserdampfes, *Z. Vereines Deutscher Ingenieure*, Vol. 60, 1916, pp. 541-546

[16] Moran, K., Inumaru, J. and Kawaji, M., Instantaneous hydrodynamics of a laminar wavy liquid film, *Int. J. Multiphase Flow*, Vol. 28, 2002, pp. 731-755